J. Fluid Mech. (2010), *vol.* 664, *pp.* 193–219. © Cambridge University Press 2010
doi:10.1017/S0022112010004027

Establishing the generality of three phenomena using a boundary layer with free-stream passing wakes

XIAOHUA WU†

Department of Mechanical Engineering, Royal Military College of Canada, Kingston, Ontario, Canada K7K 7B4

(Received 11 February 2010; revised 27 July 2010; accepted 27 July 2010; first published online 15 October 2010)

Direct numerical simulation was performed on an incompressible, smooth flat-plate boundary layer at unit molecular Prandtl number and constant surface temperature under free-stream periodically passing turbulent planar wakes over the momentum thickness Reynolds number range of $80 \leqslant Re_\theta \leqslant 1850$. This inhomogeneous free-stream wake perturbation source with mean deficit differs markedly from the isotropic turbulent patch used in the previous studies of Wu & Moin (*J. Fluid Mech.*, vol. 630, 2009, p. 5; *Phys. Fluids*, vol. 22, 2010, 085105). Preponderance of hairpin vortices is observed in both the transitional and turbulent regions of the boundary layer. In particular, the internal structure of merged turbulent spots is a hairpin forest; the internal structure of infant turbulent spots is a hairpin packet. Although more chaotic in the turbulent region, numerous hairpin vortices are readily detected in both the near-wall and outer regions of the boundary layer up to $Re_\theta = 1850$. This suggests that the hairpin vortices in the higher-Reynolds-number region are not simply the aged hairpin forests convected from the upstream transitional region. Temperature iso-surfaces in the companion thermal boundary layer are found to be a useful tracer in identifying boundary-layer hairpin vortex structures. Total shear stress overshoots wall shear stress in the transitional region and the excess relaxes gradually in the downstream turbulent region. This overshoot is shown to be associated with a localized streamwise acceleration of the streamwise velocity component. Breakdown of the wake-perturbed laminar boundary layer is closely related to the formation of hairpin packets out of quasi-streamwise vortices. Mean and second-order statistics are in good agreement with previous data on the standard turbulent boundary layer. Downstream of transition, normalized root-mean-square (r.m.s.) wall-shear-stress intensity shows almost no variation with Re_θ, whereas normalized r.m.s. wall-pressure intensity increases slightly. Taken together with the previous results of Wu & Moin, the generality of the following three phenomena in quasi-standard boundary layers can be reasonably established, namely, preponderance of hairpin vortices in the transitional as well as in the turbulent regions up to $Re_\theta = 1850$, transitional total shear stress overshoot, and a laminar-layer breakdown process closely tied to the formation of hairpin packets.

Key words: boundary layers, turbulence simulation, turbulent boundary layers

† Email address for correspondence: Xiaohua.Wu@rmc.ca

https://doi.org/10.1017/S0022112010004027 Published online by Cambridge University Press

1. Introduction

In a previous work, Wu & Moin (2009) reported direct numerical simulation (DNS) results on a nominally zero-pressure-gradient flat-plate boundary layer over the momentum thickness Reynolds number range of $80 \leqslant Re_\theta \leqslant 940$, in which the free stream is perturbed by patches of migrating isotropic turbulence. Hairpin forests were found to exist in the transitional and turbulent regions of the flow, although their turbulent region, $750 < Re_\theta < 940$, was rather short. Averaged total shear stress, τ, overshoots the averaged wall shear stress, τ_w, but the degree of excess decreases in the turbulent region with streamwise distance. Breakdown of the perturbed Blasius layer was found to be closely related to the formation of hairpin packets arising from obliquely oriented legs of upstream disjointed Λ vortices. An immediate question arising from the paper of Wu & Moin (2009) is whether the occurrence of these flow phenomena is uniquely dependent upon the type of free-stream disturbance source adopted in their simulation (Marusic 2009). Clear resolution of this question is useful for obvious reasons: the potential dominance of hairpin vortices has been at the centre of debate of boundary-layer research for several decades; the gradient of total shear stress is one relevant parameter in engineering modelling of near-wall transitional and turbulent flows, and the breakdown event marks the onset of infant turbulent spots.

Although several DNS studies on the flat-plate boundary layer were reported more recently (Castillo *et al.* 2009; Lee & Sung 2009; Li *et al.* 2009; Schlatter *et al.* 2009; Simens *et al.* 2009), the dependence of these flow phenomena on a boundary-layer disturbance source has yet to be explored, possibly due to the fact that different simulation approaches other than that of Wu & Moin (2009) were used in these more recent studies. In the simulations of Khujadze & Oberlack (2004), Schlatter *et al.* (2009) and Li *et al.* (2009), the numerical periodicity in the streamwise direction for spectral code was fulfilled by adding a fringe region at the downstream end of the computational domain, similar to the approach used by Spalart & Watmuff (1993) in their treatment of a flat-plate boundary layer under pressure gradients. In the fringe region, the outflow was forced by a prescribed volume force to the laminar Blasius inflow. In addition to triggering rapid laminar-turbulent transition, a random volume forcing directed normal to the wall was added at a short distance downstream of their inlet. Simens *et al.* (2009), Lee & Sung (2009) and Castillo *et al.* (2009), on the other hand, applied and improved the idea of recycling/re-scaling for their spatially developing boundary-layer inflow generation (Lund, Wu & Squires 1998). This is essentially a simplification of the original method of Spalart (1988). Wu & Moin (2010) increased the streamwise and spanwise dimensions used in Wu & Moin (2009) and included heat transfer, while maintaining all the other aspects of the previous simulation. Throughout the entire laminar, transitional and turbulent regions, their Stanton number to skin-friction ratio deviates from the exact Reynolds analogy value by less than 1.5 %. The turbulent Prandtl number peaks at the wall and decreases monotonically towards the boundary-layer edge with no near-wall secondary peak. It should be pointed out that in all the aforementioned numerical simulations, very good agreements with experimental data on the mean and second-order turbulent statistics were observed. However, they do not directly address the central question regarding the generality of the three observed flow phenomena.

A standard boundary layer is considered in this paper to be a zero-pressure-gradient, smooth flat-plate boundary layer with infinitesimal free stream or other types of disturbances in the sense of Schubauer & Skramstad (1947). Such a flow is regarded as a benchmark because it always proceeds in three clean stages from the

https://doi.org/10.1017/S0022112010004027 Published online by Cambridge University Press

Blasius state, through the Tollmien–Schlichting wave-dominated natural transition to turbulent. Flow physics phenomena detected from such benchmark layers should presumably be intrinsic to the boundary layer itself rather than to external sources and hence more universal. A quasi-standard boundary layer is a nominally zero-pressure-gradient, smooth flat-plate boundary layer with finite but weak free stream or other types of imposed disturbances. Phenomena detected from such flows are obviously susceptible to questioning as to their dependence on those external finite-level perturbations. A notable aspect in the quasi-standard layer of Wu & Moin (2009, 2010) compared to other DNS studies is that the Blasius state, one of the three clean stages in the benchmark layer, is retained to a good degree over a substantial distance from $Re_\theta = 80$ to approximately 180.

Aside from the central question regarding the dependence of the aforementioned three flow phenomena on the free-stream disturbance source, several additional issues also deserve clarification. It has been conjectured that the hairpin vortices observed in the turbulent region of Wu & Moin (2009) may be a result of pure advection from the aged decaying hairpin forests transported from the upstream transitional region. By the station of $Re_\theta \approx 1500$, there would be very few full hairpin vortices left in the boundary layer. Also it has been conjectured that the difference in r.m.s. wall-shear-stress fluctuation $\tau^{'+}_{w,rms}$ between Wu & Moin (2009) and DNS channel flow results is an indicator for the non-equilibrium and transitional nature of their turbulent boundary layer. Subscript w refers to wall values. Superscript ‘$'$’ represents fluctuations with respect to the mean. Superscript ‘+’ denotes normalization by the corresponding wall values. In the present work, these additional points are also addressed.

In this paper, new DNS results are reported on a quasi-standard boundary layer over the Reynolds number range of $80 \leqslant Re_\theta \leqslant 1850$. The free stream of the boundary layer is perturbed by periodically passing turbulent planar wakes. Distinctions between the present disturbance source from the isotropic turbulent patch of Wu & Moin (2009, 2010) are substantial: the wakes carry with them a finite-mean-velocity deficit (Durbin & Wu 2007); the wake turbulence is anisotropic and inhomogeneous; the wakes intersect the flat-plate boundary layer at a rather large oblique angle (see figure 1*a*,*c*). The new simulation results are used to examine the generality of the three flow phenomena previously reported by Wu & Moin (2009), and to address the related additional points. The configuration adopted here is an idealized abstraction of the wake–blade interaction problem widely studied in the turbo-machinery field (Chow, Uzol & Katz 2002; Uzol *et al.* 2003; Soranna *et al.* 2006).

2. Details of the simulation

2.1. *Computational parameters*

The momentum thickness Reynolds number of the inlet Blasius boundary layer is $Re_{\theta_0} = 80$, and the molecular Prandtl number of the incompressible fluid is $Pr = 1.0$. A temperature field, ξ, is also included in the present DNS with a constant surface temperature boundary condition. The characteristic velocity scale is the free-stream velocity outside the Blasius layer at the inlet, $U_f = 1$. Using the inlet boundary-layer momentum thickness, θ_0, as the unit length scale, the computational domain size is $L_x = 12750\theta_0$, $L_y = 2250\theta_0$ and $L_z = 562.5\theta_0$ in the streamwise, wall-normal and spanwise directions, respectively. At the streamwise station where $Re_\theta = 1410$, the computed boundary-layer thickness, δ, based on 99 % U_f, is $158\theta_0$, yielding a

https://doi.org/10.1017/S0022112010004027 Published online by Cambridge University Press

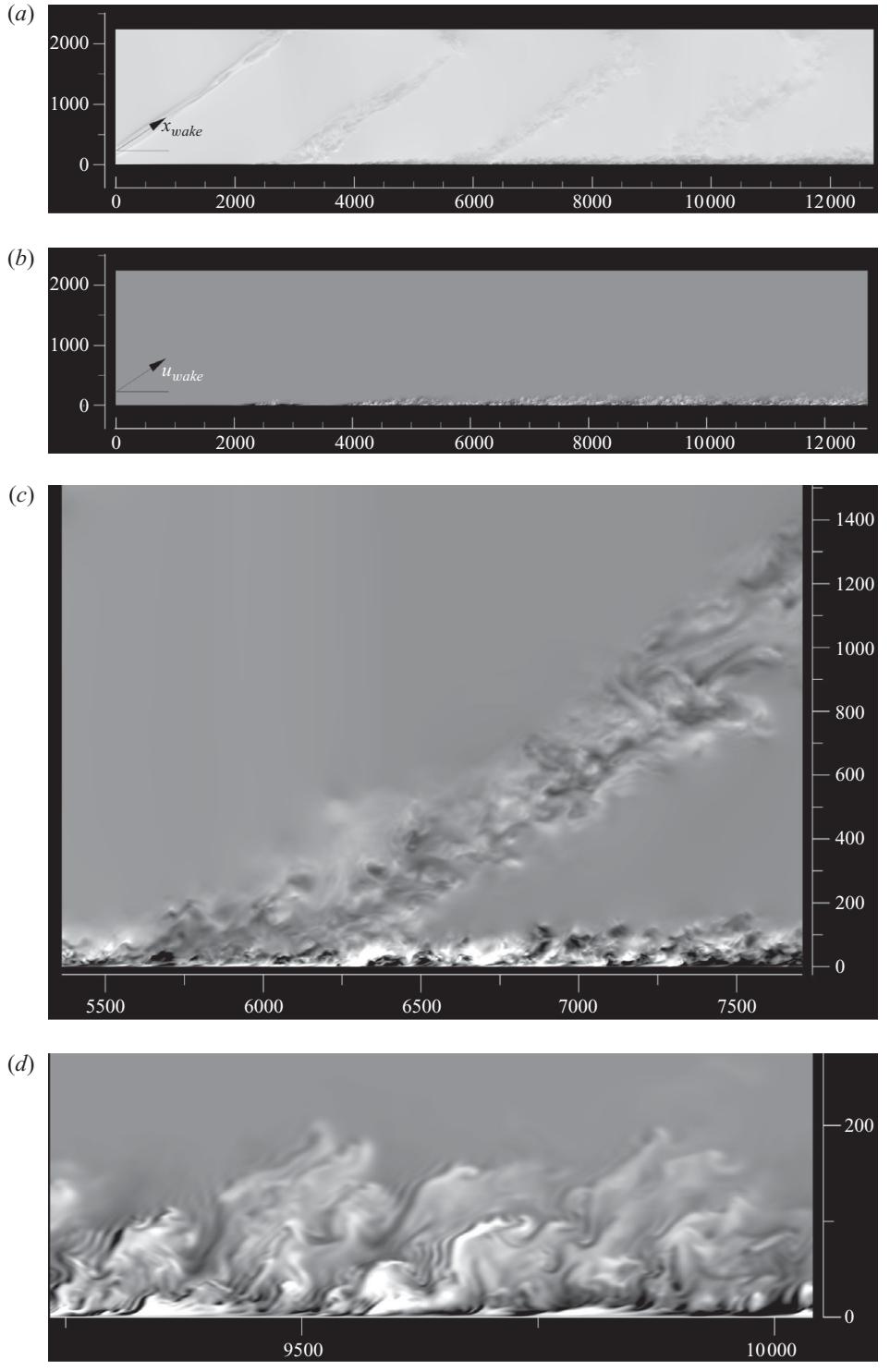


FIGURE 1. Cross-sectional view of the velocity boundary layer and thermal boundary layer with free-stream passing wakes at $t = 46\mathscr{T}$ over a random xy-plane. (*a*) $0 \leqslant u/U_f \leqslant 1.2$ with 400 levels, (*b*) $-0.2 < \phi' < 0.2$ with 100 levels, (*c*) $-0.12 < u'/U_f < 0.12$ with 400 levels (zoomed view) and (*d*) $-0.15 < \phi' < 0.15$ with 400 levels (zoomed view). White colour represents large positive values, coordinates normalized by θ_0.

https://doi.org/10.1017/S0022112010004027 Published online by Cambridge University Press

spanwise domain width to local boundary-layer thickness ratio of 3.56. At the exit of the computational domain where $Re_\theta = 1850$, this ratio is 2.72. The height of the computational domain at the exit station is 10.88δ (see figure 1).

There are 8192 and 256 grid points being distributed uniformly along the streamwise and spanwise directions, respectively, and 500 points stretched along the wall-normal direction. At the early transitional station of $Re_\theta = 250$ where skin-friction C_f is nearly at its minimum, $\Delta x^+ = 4.0$ and $\Delta z^+ = 5.6$, respectively. At the location of $Re_\theta = 750$ where C_f is nearly at its peak, $\Delta x^+ = 6.0$ and $\Delta z^+ = 8.4$, respectively. From there further downstream, the wall-unit normalized grid spacings decrease with increasing Re_θ. For example, at $Re_\theta = 1410$, $\Delta x^+ = 5.6$ and $\Delta z^+ = 7.9$. At the exit of the computational domain where $Re_\theta = 1850$, $\Delta x^+ = 5.4$ and $\Delta z^+ = 7.7$, respectively. Also at the streamwise station of $Re_\theta = 1410$, there are 18 points being distributed along the wall-normal direction below $y^+ = 10$; 44 points within the buffer region of $y^+ < 30$ and 225 points inside the boundary layer. Throughout the entire flat plate, the maximum grid spacing for the wall-normal region of $0 < y < \delta$ is less than nine wall units. The wall-normal grid distribution was generated using a small computer program developed by the late Dr Charles Pierce based on the matched hyperbolic-tangent stretching technique. The grid generator code is available upon request.

2.2. *Inlet wake prescription*

The free stream contains periodically migrating turbulent planar wakes. The inlet wake velocity field (u_{wake}, v_{wake}, w_{wake}) was obtained from a separate pre-computation of a temporally decaying turbulent planar wake (Wu *et al.* 1999). The inlet mean wake deficit is 14 % U_f and the mean wake half-width is $b = 187.5\theta_0$. The passing period, $\mathscr{T}$, was set to be $3131.45\theta_0/U_f$.

The time step throughout the entire computation was fixed at $\Delta t = \mathscr{T}/4000$. An arbitrary instant, t, corresponds to a certain fraction of the wake passing period, $t = m\mathscr{T} + n_{\mathscr{T}}\mathscr{T}$, where m is an integer corresponding to the number of elapsed periods so far and $0 \leqslant n_{\mathscr{T}} \leqslant 1$ is the fraction. On the inflow plane at the beginning of each wake passing period pre-generated planar wakes traverse from the top towards the wall at a prescribed speed of $0.7U_f$, forming an inclination angle of $\alpha = 35^\circ$ with respect to the flat plate. Depending upon the passing period, $\mathscr{T}$, at any given instant either one single wake or multiple wakes can be found on the inflow plane. A wake will be found on the computational inflow plane if its centreline is located within the range from $y = -b/\cos\alpha$ to $y = L_y + b/\cos\alpha$. The total number of such wakes at any time is

$$\mathscr{N} = \mathrm{CEILING}\left(\frac{L_y + 2b/\cos\alpha}{U_f\mathscr{T}\tan\alpha}\right), \tag{2.1}$$

where the function CEILING returns the least integer greater than or equal to its real argument. On the inflow plane at the beginning of a new wake passing period $n_{\mathscr{T}} = 0$, let the centreline of the qth wake, i.e. the origin of this particular wake coordinate system ($x_{wake} = 0$, $y_{wake} = 0$), start to move downward from $y = L_y + b/\cos\alpha$. At any subsequent instant with fraction $n_{\mathscr{T}}$, the y-coordinate of the centreline of this particular wake will be $L_y + b/\cos\alpha - n_{\mathscr{T}}\mathscr{T}U_f\tan\alpha$. The velocity field of this qth wake can therefore be interpolated into every point on the inflow plane, yielding $u_{eff,wake,q}$, $v_{eff,wake,q}$ and $w_{eff,wake,q}$. The subscript '*eff*, *wake*, q' represents the contributions from the qth wake to the velocity field on the inlet yz-plane. The velocity components and

https://doi.org/10.1017/S0022112010004027 Published online by Cambridge University Press

temperature over the $x=0$ plane are finally prescribed as

$$\left.\begin{array}{ll} u = u_{Blasius} + \left(\cos\alpha \sum_{q=1}^{\mathscr{N}} u_{eff,wake,q} - \sin\alpha \sum_{q=1}^{\mathscr{N}} v_{eff,wake,q}\right), & \text{if } y > 46.15\theta_0 \\ u = u_{Blasius}, & \text{otherwise.} \end{array}\right\} \quad (2.2)$$

$$\left.\begin{array}{ll} v = v_{Blasius} + \left(\sin\alpha \sum_{q=1}^{\mathscr{N}} u_{eff,wake,q} + \cos\alpha \sum_{q=1}^{\mathscr{N}} v_{eff,wake,q}\right), & \text{if } y > 46.15\theta_0 \\ v = v_{Blasius}, & \text{otherwise.} \end{array}\right\} \quad (2.3)$$

$$\left.\begin{array}{ll} w = \sum_{q=1}^{\mathscr{N}} w_{eff,wake,q}, & \text{if } y > 46.15\theta_0 \\ w = 0, & \text{otherwise.} \end{array}\right\} \quad (2.4)$$

$$\phi = \phi_{Blasius}, \quad (2.5)$$

where subscript '*Blasius*' denotes the Blasius solution and u, v and w are the instantaneous velocity components along the streamwise, wall-normal and spanwise directions, respectively. As indicated, the front of the traversing planar wake is restricted to be six inlet boundary-layer thicknesses ($46.15\theta_0$) away from the flat plate. The reason for this design is so that the Blasius boundary layer at the inlet remains undistorted by the imposed perturbations and therefore avoids the arbitrariness in prescribing the perturbed velocity profile inside the layer. This design has the added benefit of ensuring that disturbances inside the boundary layer originate from the free stream rather than from upstream.

All the other boundary conditions, initial conditions, geometrical parameters, governing equations and numerical method are identical to those documented in Wu & Durbin (2000). The readers are directed to that paper for a thorough description. The computation was performed on a Sun SPARC Enterprise M9000 Sever with 160 shared-memory threads for a total of $250\,000\Delta t$ with a total consumption of approximately one million CPU hours. Statistics were sampled for a duration of $125\,000\Delta t$. The maximum component Courant–Friedrichs–Lewy number, defined as $\Delta t(|u|/\Delta x + |w|/\Delta z)$, was approximately 0.72 during the run.

3. Description of the boundary layer

Undistorted images of the velocity and thermal boundary layers at $t = 46\mathscr{T}$ over one random xy-plane are shown in figure 1. Figures 1(a) and 1(b) present a full planar view of the flow, but with unclear details. This is remedied in figures 1(c) and 1(d), which give a close-up view of the velocity and thermal boundary layers with interesting flow structures. From the velocity contours of figure 1(a), it can be seen that there is some degree of spreading of the free-stream wakes. The oblique wake inclination angle with respect to the flat plate, i.e. the $y=0$ plane, is, however, maintained during the streamwise development of the free-stream wakes. Based on the velocity contours of figures 1(a) and 1(c), it is apparently difficult to separate the free-stream perturbation from the wall turbulence. This is, however, easily achieved through the contours of ϕ' shown in figures 1(b) and 1(d). The non-dimensional temperature, ϕ, is defined as $\phi = (\xi - \xi_{ref})/(\xi_w - \xi_{ref})$: see Wu & Durbin (2000).

https://doi.org/10.1017/S0022112010004027 Published online by Cambridge University Press

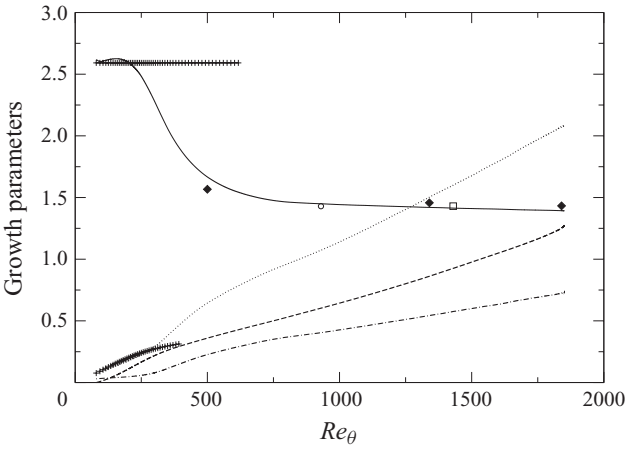


FIGURE 2. Growth parameters of the present boundary layer with free-stream passing wakes. Lines are DNS results. Dotted, $10^{-2}\delta/\theta_0$; dashed, $10^{-4}x/\theta_0$; solid, H; dash-dotted, $10^{-3}Re_\tau$. Plus, Blasius solutions; diamond, Purtell, Klebanoff & Buckley (1981); circle, Adrian *et al.* (2000); square, DeGraaff & Eaton (2000).

Here $\xi_{ref}=0$ is the temperature at the top boundary of the computational domain; subscript w again refers to wall values.

The inclusion of thermal boundary layer in the present DNS was inspired by the classical wind-tunnel boundary-layer work of Chen & Blackwelder (1978), Van Atta & Helland (1980), Gad-el-Hak, Blackwelder & Riley (1981) and Murlis, Tsai & Bradshaw (1982). Chen & Blackwelder (1978) found the use of a small amount of heat as a passive contaminant to be a valuable technique for studying the large-scale coherent motions in the standard boundary layer. By uniformly heating the boundary layer from its beginning, the heat served as a tracer for the turbulence. With low heat flux, the dynamical structures in the shear layer were virtually unchanged. Van Atta & Helland (1980) reasoned that since velocity measurements were not able to provide a full picture of the paths of fluid particles in the transitional boundary layer, it was logical to think that tagging the fluid with a passive scalar, like heat, could eventually shed some light on the development of turbulent spots in the transitional layer. Murlis *et al.* (1982) also heated their flat plate in the study of boundary-layer intermittency. They commented that the temperature-based intermittency discrimination schemes are superior for measuring turbulent/non-turbulent zone-length statistics compared to velocity-based schemes.

Parameters characterizing the streamwise growth of the boundary layer are presented in figure 2. At the station of $Re_\theta=1410$, the friction-velocity-based Reynolds number $Re_\tau=u_\tau\delta/\nu=568$; at the station of $Re_\theta=1800$, $Re_\tau=708$. Because of the mean velocity deficit carried by the inlet passing wakes, there is already noticeable deviation from the Blasius value of shape factor, H, in the laminar region near the inlet. In comparison, in the work of Wu & Moin (2009, 2010), where the free-stream isotropic turbulent patches carry zero mean velocity, such deviation is negligibly small. However, it should be pointed out that the current deviation level, although finite, is still not significant. After transition, good agreement with experimental data on H is seen in the turbulent region. Figure 2 also shows that, at the station of $x/\theta_0=10\,000$, the corresponding Reynolds number is $Re_\theta=1532$; at $x/\theta_0=11\,000$, $Re_\theta=1670$. The

https://doi.org/10.1017/S0022112010004027 Published online by Cambridge University Press

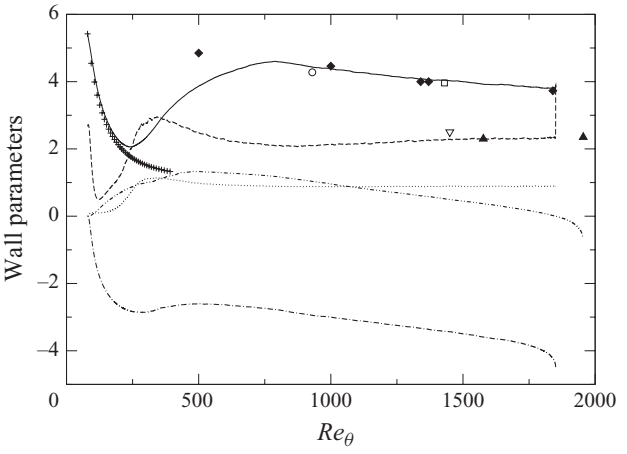


FIGURE 3. Wall parameters of the present boundary layer with free-stream passing wakes. Lines are DNS results. Solid, $10^3 C_f$; dashed, $p'^+_{w,rms}$; dotted, $2\tau'^+_{w,rms}$; dash-dotted, $10^2 C_{pw}$. Plus, Blasius solution; diamond, Purtell *et al.* (1981); circle, Adrian *et al.* (2000); square, DeGraaff & Eaton (2000); up-triangle, Gravante *et al.* (1998); down-triangle, Schewe (1983); dash-dotted-dotted, $10^2 C_{pw}$ from Wu & Moin (2010).

streamwise location of $Re_\theta = 1800$ is found at $x/\theta_0 = 12\,090$. This information is useful in subsequent flow visualization studies.

Analogous to the shape factor, H, the skin-friction coefficient $C_f = 2\tau_w/\rho U_f^2$ in the present boundary layer departs from the Blasius profile starting from the inlet (figure 3). In contrast, the C_f from Wu & Moin (2009) collapses on the Blasius curve until $Re_\theta = 180$. After transition downstream of $Re_\theta = 800$, the present C_f is in good agreement with the experiments as shown in the figure. Wall-static pressure coefficient $C_{pw} = 2[\overline{p}_w(x) - \overline{p}_w(x=0)]/\rho U_f^2$ for the present flow is also contrasted with that from Wu & Moin (2010) in figure 3. In this paper, an overbar indicates averaging over time as well as over the spanwise direction. It is seen that downstream of $Re_\theta = 300$, the two C_{pw} curves display analogous streamwise variations, indicating similar levels of streamwise pressure gradient. The difference lies in the region of $80 < Re_\theta < 300$ in which the two boundary layers exhibit opposite signs of streamwise pressure gradient. It should, however, be pointed out that the implied streamwise pressure gradient is still nominally zero, since the C_{pw} results displayed in the figure have been multiplied by a factor of 100. Figure 3 also indicates that the r.m.s. wall-pressure fluctuation $p'^+_{w,rms}$ increases slowly with Re_θ, whereas the r.m.s. wall-shear fluctuation $\tau'^+_{w,rms}$ is nearly constant from $750 < Re_\theta < 1800$. This is in agreement with Wu & Moin (2010) both quantitatively and qualitatively, and demonstrates the fact that equilibrium values of $\tau'^+_{w,rms}$ have indeed been achieved in the two boundary layers. Furthermore, the equilibrium values are insensitive to the types of free-stream disturbance used in the two flows.

Figure 4 presents the mean velocity and its wall-normal derivative at two Reynolds numbers. The results at $Re_\theta = 1410$ are in good agreement with the DNS of Spalart (1988). Logarithmic dependence of the normalized mean velocity on y^+ is approximately achieved within the narrow range of $50 < y^+ < 90$. Furthermore, the collapse between the profiles of $\overline{u}^+$ and $\mathrm{d}\overline{u}^+/\mathrm{d}\ln y^+$ for $y^+ < 3$ indicates that the anticipated linear dependence of $\overline{u}^+$ on y^+ is accurately captured by the present DNS. Turbulence intensities at $Re_\theta = 1410$ and 1750 from the present DNS are compared

https://doi.org/10.1017/S0022112010004027 Published online by Cambridge University Press

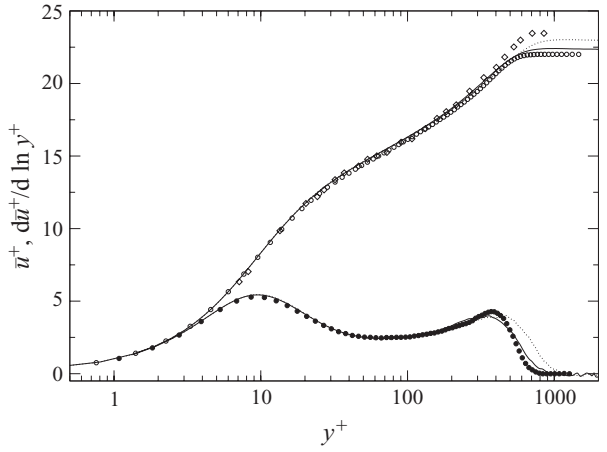


FIGURE 4. Wall-normal profiles of mean velocity, $\overline{u}^+$, and derivative, $\mathrm{d}\overline{u}^+/\mathrm{d}\ln y^+$, in the boundary layer with passing wakes. Solid line, DNS at $Re_\theta = 1410$; dotted line, DNS at $Re_\theta = 1750$; circle, DNS of Spalart (1988) at $Re_\theta = 1410$; diamond, DNS of Purtell *et al.* (1981) at $Re_\theta = 1840$.

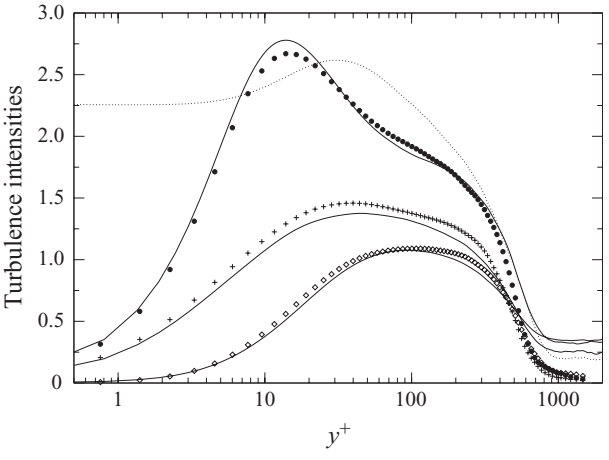


FIGURE 5. Wall-normal profiles of turbulence intensities at $Re_\theta = 1410$ in the boundary layer with passing wakes. Lines are present DNS results; symbols are from Spalart (1988). Circle, u'^+_{rms}; diamond, v'^+_{rms}; plus, w'^+_{rms}; dotted line, p'^+_{rms}.

with the DNS of Spalart (1988) and with the experimental data of Karlsson & Johansson (from Osterlund 1999) in figures 5 and 6, respectively. Agreements are very good inside the inner 70 % of the boundary layer. Towards the boundary-layer edge and also in the free stream, the current profiles show the anticipated higher levels of residual fluctuations arising from the passing turbulent wakes. The increase in $p'^+_{w,rms}$ from 2.25 in figure 5 to 2.3 in figure 6 is already implied by figure 3. This increasing trend is consistent with the pipe flow results of Wu & Moin (2008) in which $p'^+_{w,rms}$ increases from 1.7 at $Re_D = 5300$ to 2.5 at $Re_D = 44\,000$. The results of the previous three figures suggest that, except for a region near the boundary-layer edge, the present wake-perturbed quasi-standard turbulent boundary layer shares similar

https://doi.org/10.1017/S0022112010004027 Published online by Cambridge University Press

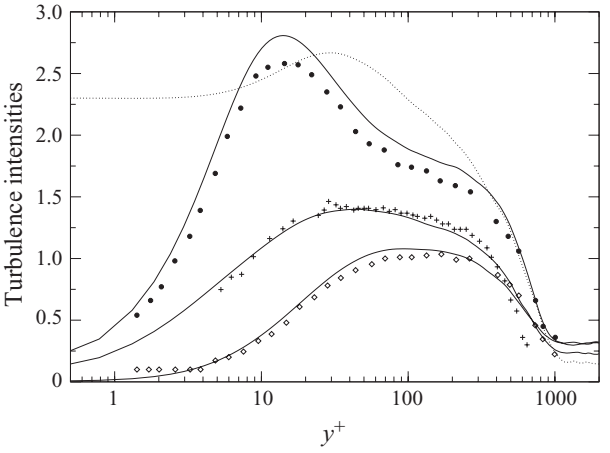


FIGURE 6. Wall-normal profiles of turbulence intensities at $Re_\theta = 1750$ in the boundary layer with passing wakes. Lines are present DNS results; symbols are from Karlsson & Johansson at $Re_\theta = 2420$; as in Osterlund (1999). Circle, u'^+_{rms}; diamond, v'^+_{rms}; plus, w'^+_{rms}; dotted line, p'^+_{rms}.

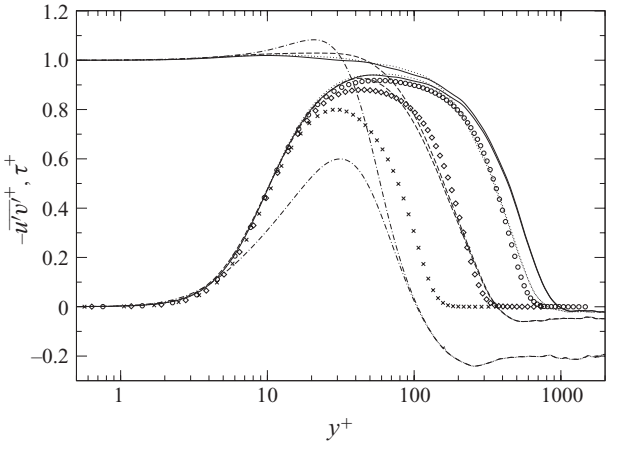


FIGURE 7. Wall-normal profiles of Reynolds shear stress and total shear stress in the boundary layer with free-stream passing wakes. DNS of Spalart (1988): circle, $Re_\theta = 1410$; diamond, 670; cross, 300. Present DNS: solid line, $Re_\theta = 1750$; dotted, 1410; dashed, 670; dash-dotted, 300.

mean velocity and second-order statistical characteristics with other classic turbulent flat-plate boundary layers.

4. Total shear stress overshoot

Reynolds shear stress and total shear stress profiles from the present DNS at $Re_\theta = 300$, 670, 1410 and 1750 are shown in figure 7. The set of results converging to zero at the wall is $-\overline{u'v'}^+$, whereas the set of lines approaching one at the wall is τ^+. The lower three Reynolds numbers were chosen to be the same as those in Spalart (1988) so that a comparison with his Reynolds shear stress data can be made. Since the present DNS is still in the process of transition at the lowest Reynolds-number station, a comparison at $Re_\theta = 300$ is actually not meaningful. At

https://doi.org/10.1017/S0022112010004027 Published online by Cambridge University Press

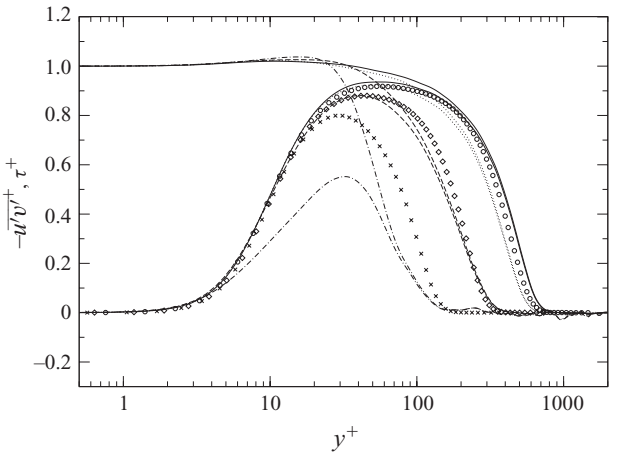


FIGURE 8. Reynolds shear stress and total shear stress profiles from the simulation of Wu & Moin (2010). $-\overline{u'v'}^+$ from Spalart (1988): circle, $Re_\theta = 1410$; diamond, 670; cross, 300. Wu & Moin: solid, $Re_\theta = 1750$; dotted, 1410; dashed, 670; dash-dotted, 300.

the other two stations, the comparisons are quite reasonable. In the free stream, the present $-\overline{u'v'}^+$ attains negative values due to the orientation of the inhomogeneous turbulent passing wakes (Wu *et al.* 1999; Uzol *et al.* 2003). The total shear stress profile has an 8 % overshoot at $Re_\theta = 300$ with rapid relaxation downstream. The wall-normal gradient of the total shear stress at the wall is still zero, as expected from (4.1). Results at the same four Reynolds number stations extracted from the recent simulation data of Wu & Moin (2010) are shown in figure 8. Wu & Moin (2010) extended the streamwise extent of the previous DNS of Wu & Moin (2009), but maintained the old simulation design. Without the presence of the passing wakes, the Reynolds shear stress levels in figure 8 decrease to zero in the free stream. The profile at $Re_\theta = 300$ in figure 8 seems to suggest a lower degree of overshoot in Wu & Moin (2010). However, figure 9 shows that the maximum level of overshoot is nearly the same in these two flows with the maximum being achieved at $Re_\theta \approx 350$ in Wu & Moin (2010) rather than at 300. Overall, the results presented in the previous two figures convincingly demonstrate the generality of the total shear stress overshoot phenomena in transitional quasi-standard boundary layers.

It would be useful to understand the statistical factor contributing to this overshoot. Figure 10 presents the right-hand side terms of (4.1), each contributing to the wall-normal gradient of the total shear stress. The results are at the streamwise station of $Re_\theta = 300$ for the present wake-perturbed boundary layer, where

$$\frac{\partial}{\partial y}\left(\nu\frac{\partial \overline{u}}{\partial y} - \overline{u'v'}\right) = \overline{u}\frac{\partial \overline{u}}{\partial x} + \overline{v}\frac{\partial \overline{u}}{\partial y} + \frac{1}{\rho}\frac{\partial \overline{p}}{\partial x} - \nu\frac{\partial^2 \overline{u}}{\partial x^2} + \frac{\partial \overline{u'^2}}{\partial x}. \tag{4.1}$$

It is obvious from the figure that the near-wall positive gradient of total shear stress is correlated with the positive contribution from $\overline{u}\partial\overline{u}/\partial x$ in the region of $y^+ < 22$. The viscous term and the pressure-gradient term are negligibly small. The streamwise gradient of $\partial\overline{u'^2}/\partial x$ also makes a positive contribution to the overshoot, but is not the deciding factor. The wall-normal gradient term $\overline{v}\partial\overline{u}/\partial y$ does not contribute positively to the total shear stress overshoot. Figure 11 shows profiles of $\overline{u}\partial\overline{u}/\partial x$

https://doi.org/10.1017/S0022112010004027 Published online by Cambridge University Press

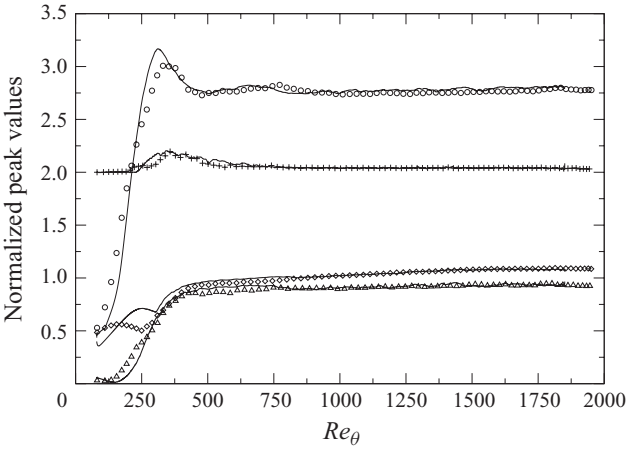


FIGURE 9. Variations of normalized peak turbulence intensities, Reynolds stresses and total shear stress with Re_θ. Lines are present DNS; symbols are from Wu & Moin (2010). Circle, $u^{'+}_{rms,peak}$; diamond, $v^{+}_{rms,peak}$; triangle, $-\overline{u'v'}^{+}_{peak}$; plus, $2\tau^{+}_{peak}$.

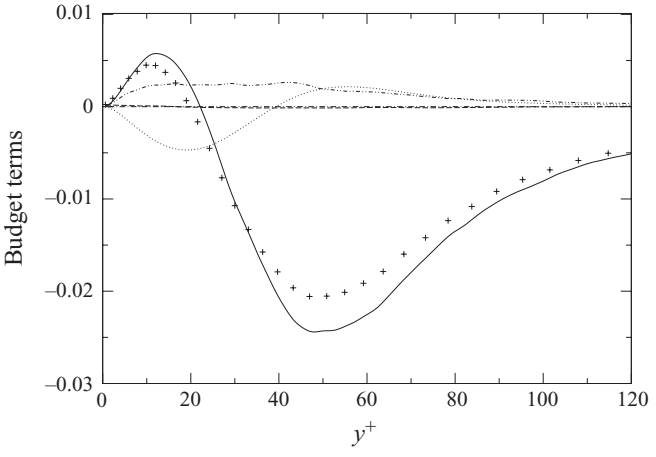


FIGURE 10. Right-hand side budget terms of (4.1) in the boundary layer with passing wakes at $Re_\theta = 300$ multiplied by ν/u_τ^3. Solid, $\overline{u}\partial\overline{u}/\partial x$; dotted, $\overline{v}\partial\overline{u}/\partial y$; dashed, $1/\rho\partial\overline{p}/\partial x$; dash-dotted, $-\nu\partial^2\overline{u}/\partial x^2$; dash-dotted-dotted, $\partial\overline{u'^2}/\partial x$; plus, summation.

and the summation term of (4.1) at four streamwise stations extracted from the data of Wu & Moin (2010) in which the free stream is traversed by isotropic turbulent patches. The strong dependence of $\partial\tau/\partial y$ on the streamwise acceleration term $\overline{u}\partial\overline{u}/\partial x$ is again evident. Thus, localized (below the buffer layer) streamwise acceleration of the streamwise velocity component in the transitional region downstream of the breakdown event is the main contributor to the total shear stress overshoot in transitional quasi-standard boundary layers.

5. Preponderance of hairpin vortices

The planar view of the thermal boundary layer at $t = 46\mathscr{T}$ in figure 1(*b*) suggests the presence of turbulent spot(s) within the streamwise range of $2000 < x/\theta_0 < 3200$.

https://doi.org/10.1017/S0022112010004027 Published online by Cambridge University Press

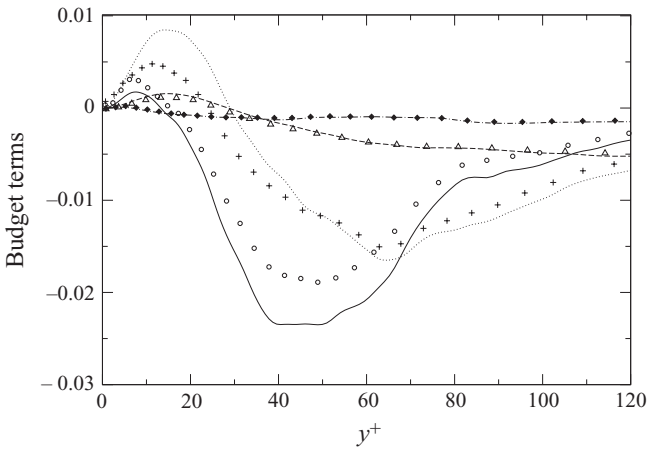


FIGURE 11. Right-hand side budget terms of (4.1) multiplied by ν/u_τ^3 using the data of Wu & Moin (2010). The $\overline{u}\partial\overline{u}/\partial x$ term: solid, $Re_\theta = 300$; dotted, 375; dashed, 670; dash-dotted, 1410. The summation term: circle, $Re_\theta = 300$; plus, 375; triangle, 670; diamond, 1410.

The actual turbulent spots and their internal structures are revealed in figure 12(a) using the second invariant of the velocity gradient tensor (Q). From the figure, the existence of two turbulent spots can be discerned, the larger one obviously a merger of several earlier individual spots. The two turbulent spots cover approximately a Reynolds number range of $300 < Re_\theta < 400$, equivalent to 20–25 local boundary-layer thicknesses. The densely populated hairpin vortices revealed by the iso-surfaces of $Q \approx 0$ inside the present passing-wake-induced turbulent spots are quite similar to those observed by Wu & Moin (2009, 2010) with free-stream blocks of isotropic turbulence.

Since the passive scalar equation was also solved in the present DNS, visualization of the temperature field in the turbulent spots of figure 12(a) is a logical next step. The temperature iso-surfaces shown in figure 12(b) are at $\phi = 0.08$, a small value but still sufficiently away from any potential minute numerical temperature oscillations around zero in the free stream. ϕ in the free stream should be exactly zero as dictated by the top-surface boundary condition. Changing the iso-surface value to $\phi = 0.05$ makes small differences in the resulting image. The structures revealed by figure 12(b) are interesting and bear a certain degree of resemblance to the hairpin structures detected in figure 12(a) using the $Q \approx 0$ iso-surfaces. These hairpin-shaped temperature iso-surfaces are also consistent with the transport effect of actual hairpin vortices on the passive scalar field. Detailed and more concrete connections of these three entities will be discussed later using figures 14 and 15.

Figure 13(a–c) shows iso-surfaces of $\phi = 0.08$ in the present passing-wake perturbed boundary layer downstream of the individual turbulent spots of figure 12. The hairpin-shaped temperature iso-surfaces in figure 13(a) ($470 < Re_\theta < 830$) are clearly less chaotic, as expected, than those in figure 13(c) ($1210 < Re_\theta < 1550$). Preponderance of hairpin vortices in the turbulent region up to $Re_\theta = 1830$ is forcefully demonstrated in figure 14(a) using iso-surfaces of $Q \approx 0$. A hairpin forest is observed. Figure 14(b) shows the temperature iso-surfaces of $\phi = 0.05$ over the same region. In order to demonstrate that these thermal structures are indeed effects of hairpin vortices on the passive temperature field, one hairpin-shaped structure was randomly identified in figure 14 with an inserted arrowhead. The definition for a vortex used in this paper

https://doi.org/10.1017/S0022112010004027 Published online by Cambridge University Press

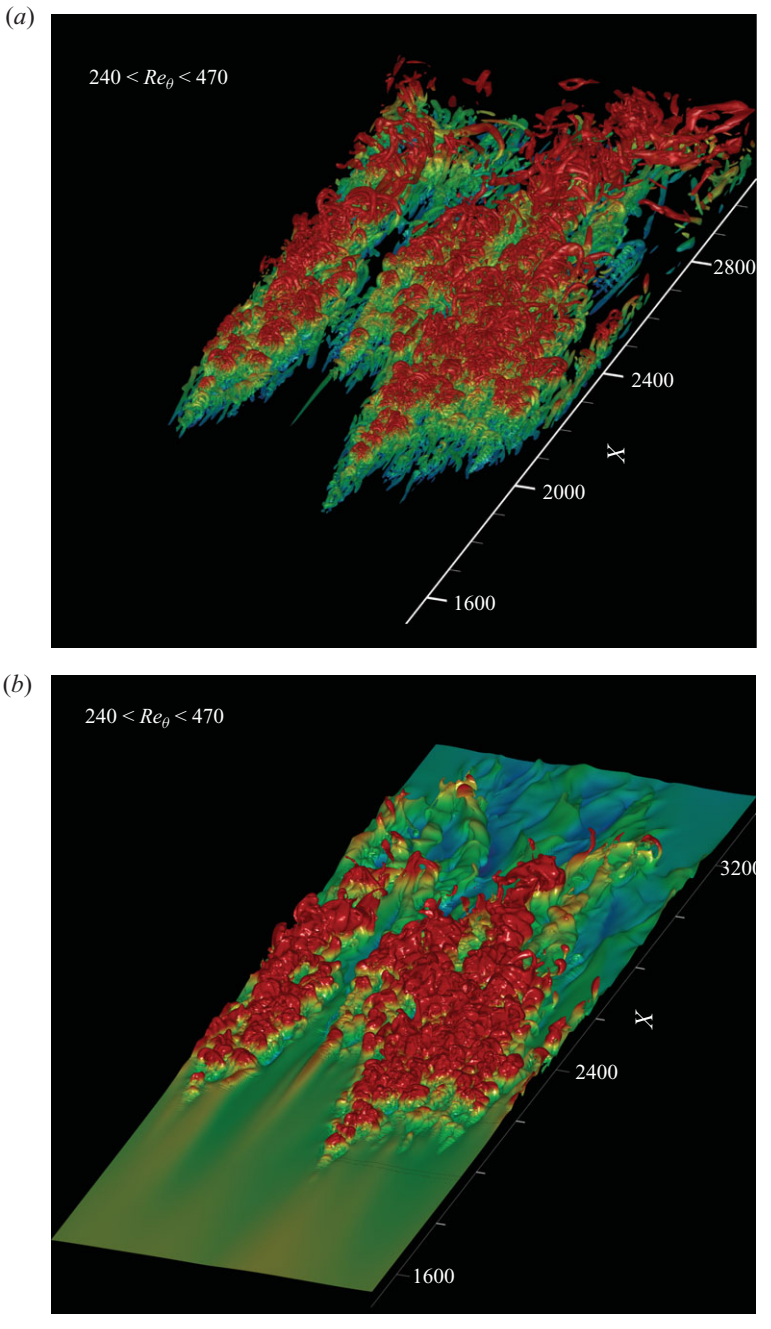


FIGURE 12. Visualization of the merged turbulent spots in the boundary layer with passing wakes at $t = 46\mathscr{T}$. (*a*) Iso-surfaces of the second invariant of the velocity gradient tensor, $Q \approx 0$. (*b*) Iso-surfaces of $\phi = 0.08$. The iso-surfaces are coloured with local values of y/δ using the same scales as in figure 13(*c*).

is the same as that used by Zhou *et al.* (1999). A vortex exists when instantaneous streamlines mapped onto a plane normal to the vortex core exhibit a roughly circular or spiral pattern, when viewed from a frame moving with the centre of the vortex

https://doi.org/10.1017/S0022112010004027 Published online by Cambridge University Press

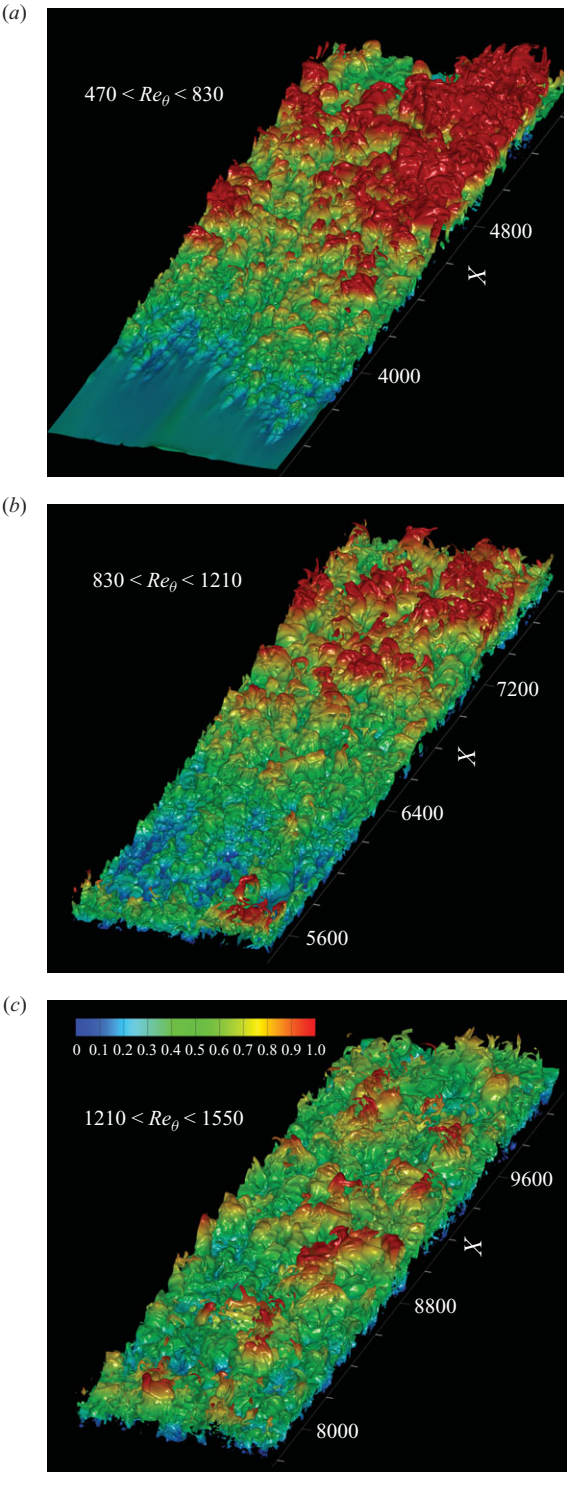


FIGURE 13. Iso-surfaces of $\phi = 0.08$ coloured using local values of y/δ in the boundary layer with passing wakes at $t = 46\mathscr{T}$. (*a*) $470 < Re_\theta < 830$, (*b*) $830 < Re_\theta < 1210$ and (*c*) $1210 < Re_\theta < 1550$.

https://doi.org/10.1017/S0022112010004027 Published online by Cambridge University Press

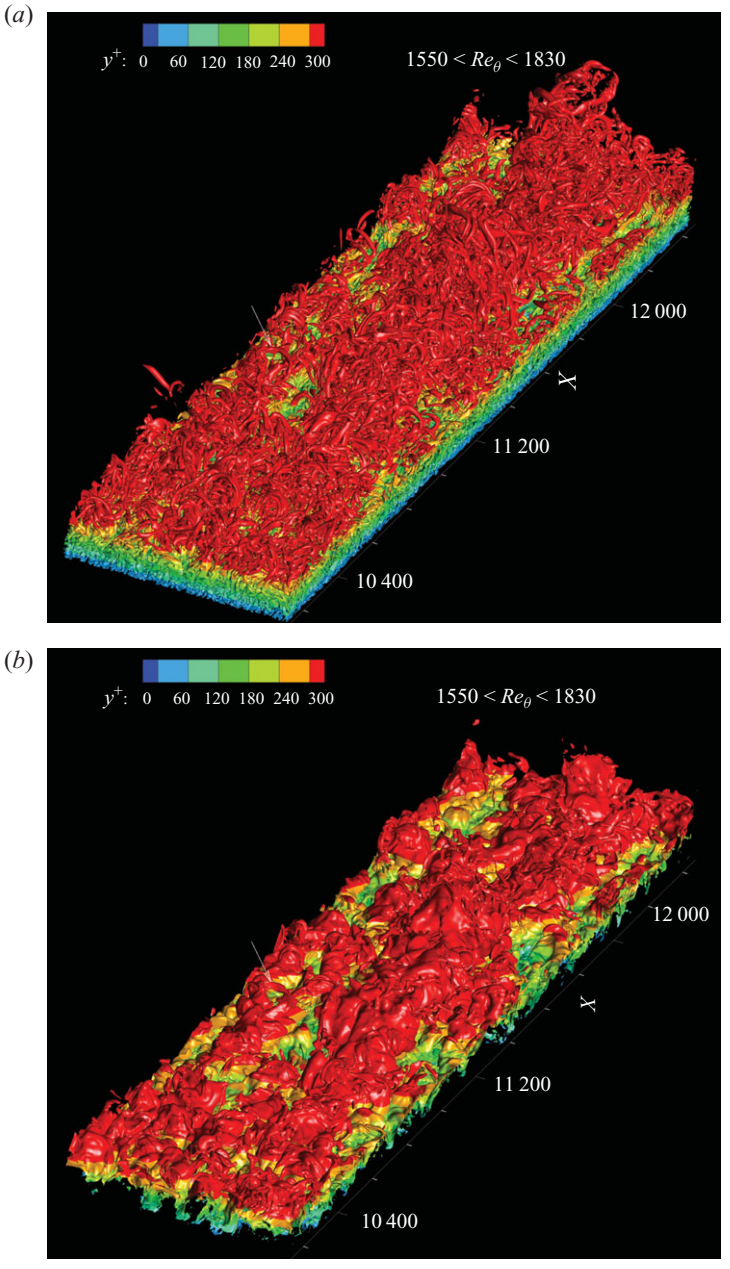


FIGURE 14. Comparison of structures resolved using Q and temperature over $1550 < Re_\theta < 1830$ in the boundary layer with passing wakes at $t = 46\mathscr{T}$. Iso-surfaces are coloured using local values of y^+. (*a*) $Q \approx 0$ and (*b*) $\phi = 0.05$.

core. Figures 15(*a*) and 15(*b*) show the local instantaneous vortex lines overlaid on the hairpin-shaped structures identified with $Q \approx 0$ and $\phi = 0.05$, respectively. The instantaneous vortex lines shown in figure 15 provide direct evidence that the hairpin-shaped iso-surface structures in figures 14(*a*) and 14(*b*) indeed correspond to well-defined hairpin vortices. The direct approach used in figure 15 for hairpin vortex detection is similar to that of Moin & Kim (1985) and Kim & Moin (1986),

https://doi.org/10.1017/S0022112010004027 Published online by Cambridge University Press

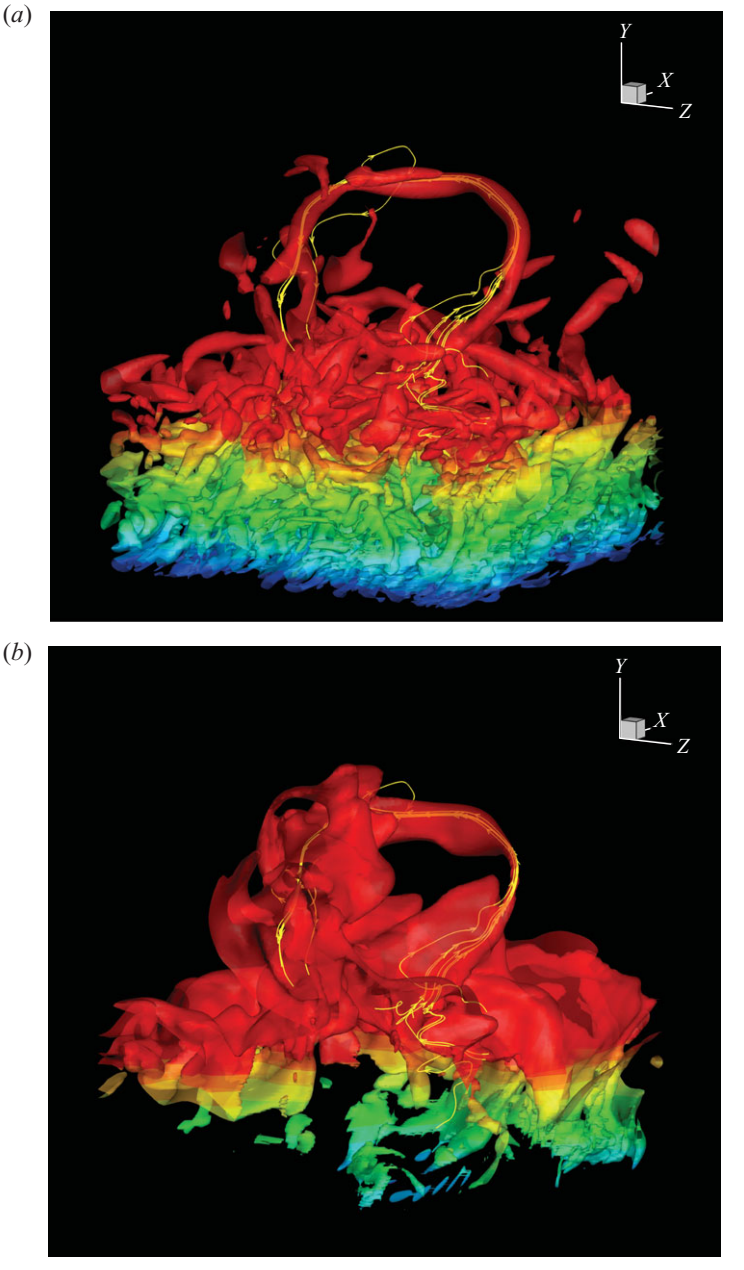


FIGURE 15. Zoomed view of the highlighted hairpin structure in figure 14 overlaid with local instantaneous vortex lines. (*a*) $Q \approx 0$ and (*b*) $\phi = 0.05$.

and is also quite analogous to the velocity-vector-based method used by Adrian, Meinhart & Tomkins (2000) and Adrian (2007) in processing their particle image velocimetry experimental data (see also Wallace 2009).

The hairpin-shaped thermal iso-surfaces shown in figures 12–15 correspond to temperature values at least 5 % of the wall temperature, ϕ_w; a level sufficiently away from those can potentially be contaminated by any minute numerical temperature oscillations in the free stream with respect to $\phi_{ref} = 0$. As correctly pointed out by

https://doi.org/10.1017/S0022112010004027 Published online by Cambridge University Press

one of the referees, one should exercise caution in choosing very small values for the temperature iso-surfaces. One should also realize that, although widely accepted, the second invariant of the velocity gradient tensor is only an indirect imperfect detector of vortex motion. It can potentially suffer from numerical effects. See, for example, as pointed out by the referee, figure 12(*a*), near the right edge at $x/\theta_0 \approx 2050$ and 2250.

The numerous hairpin-shaped temperature iso-surface bulges shown in figures 12(*b*), 13 and 14(*b*) can, therefore, be attributed to a preponderance of hairpin vortices in the present quasi-standard transitional and turbulent boundary layer up to $Re_\theta = 1850$. Strong evidence for the continued existence of a hairpin forest in the turbulent region is found in figure 14(*a*) using $Q \approx 0$. Furthermore, taken together with the results of Wu & Moin (2009, 2010), this preponderance is insensitive to the types of (intermittent) disturbance sources involved in the upstream bypass transition process.

6. Small-scale hairpins in the near-wall region

It was conjectured that the preponderance of hairpin vortices reported by Wu & Moin (2009) in their turbulent region might be a result of pure advection from the hairpin forests in their upstream transitional region. It was also conjectured that by the station of perhaps $Re_\theta \approx 1500$, there would be only very few full hairpins left in the boundary layer as remnants of the decayed upstream hairpin forest. The earlier visualizations in figures 13–15 have already provided evidence for the above conjectures. Here, additional evidence is supplied.

Figure 16(*a*) attempts to visualize the structures in an intermediate region between the outer layer and the wall. The level for the iso-surfaces of Q in the figure is 10 times larger than that in figure 14(*a*). The structures are coloured by local values of y^+. Numerous hairpin structures located in the range of $0 < y^+ < 300$ are revealed, which demonstrates the preponderance of hairpin vortices beneath the outer layer for $Re_\theta > 1500$. At $Re_\theta = 1800$, $Re_\tau = 708$. In figure 16(*b*), the iso-surface level further increases to a value 30 times larger than that in figure 14(*a*). Structures of further smaller scales are revealed. One such small hairpin-shaped structure is highlighted in figure 16(*b*) with an arrowhead. Local instantaneous vortex lines are overlaid on this structure in figure 17. It is seen that the structure indeed represents a small, well-defined hairpin vortex extending from the wall to $y^+ \approx 100$.

In order to detect near-wall structures using temperature iso-surfaces instead of Q, two approaches are explored in this study. Firstly, the entire temperature field was reset to zero at some arbitrary point. With the resumption of the simulation, a fresh thermal boundary layer initiates from the wall. The growth of the new thermal layer starting from the wall mimics, to certain extent, the release of pre-laid thin sheets of dye into the flow from the wall (Gad-El-Hak *et al.* 1981). Small hairpin-shaped temperature iso-surfaces were found and traced in the newly developed young thermal layer. The other approach is to simply adopt a relatively high level of ϕ closer to the wall value. Figure 18 presents the iso-surfaces of $\phi = 0.28$ over the streamwise range of $1671 < Re_\theta < 1825$. The iso-surfaces are coloured using local values of y^+. Many hairpin-shaped bulges are visible in the figure with one being randomly selected. Figure 19 overlays the local instantaneous vortex lines on the highlighted temperature bulge of figure 18. The vortex lines confirm the existence of a hairpin vortex in the wall-normal range of $0 < y^+ < 100$.

It is, therefore, quite clear that there exist many small-scale hairpin vortices in the near-wall region beneath the outer layer. This evidence is contrary to the 'advection-and-disappear' conjecture which was proposed regarding the work of Wu & Moin

https://doi.org/10.1017/S0022112010004027 Published online by Cambridge University Press

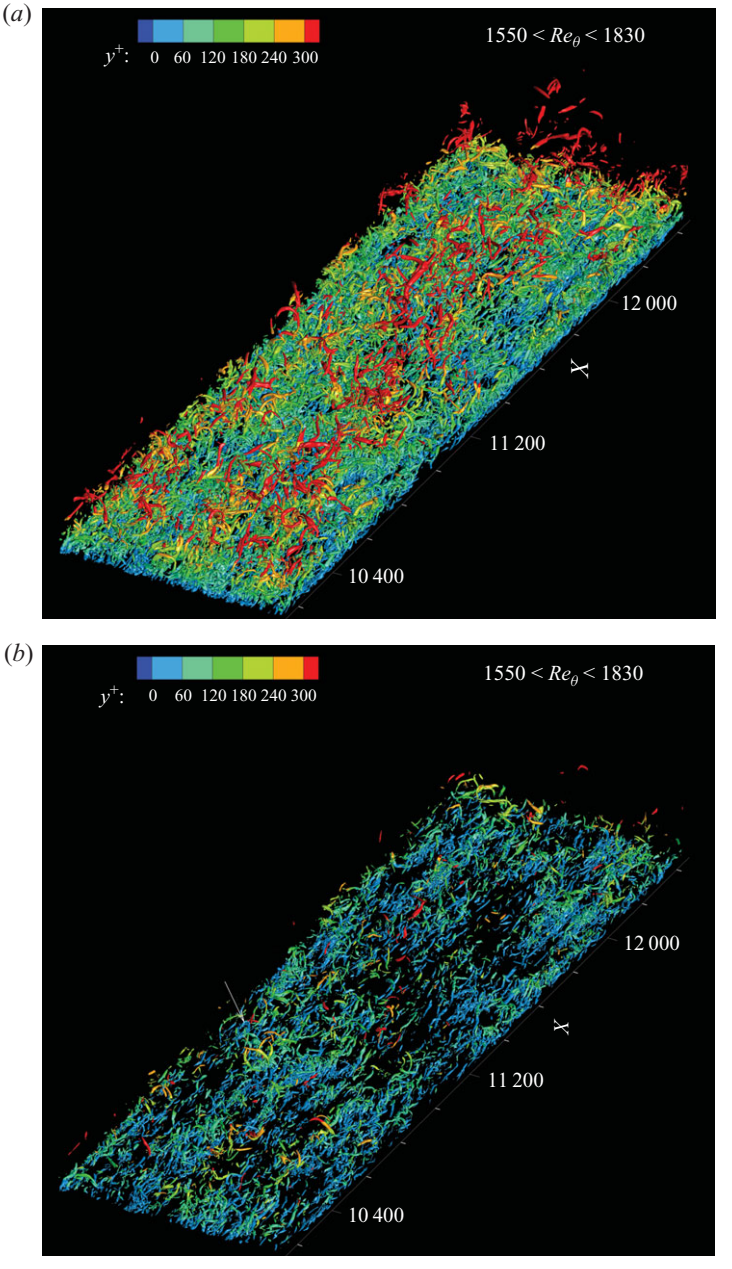


FIGURE 16. Near-wall small structures resolved by Q in the boundary layer with passing wakes at $t = 46\mathscr{T}$. Iso-surfaces are coloured using local values of y^+. (*a*) Threshold level: 10 times larger than that in figure 14(*a*). (*b*) Threshold level: 30 times larger than that in figure 14(*a*).

(2009), but quite consistent with the auto-generation mechanism advanced by Zhou *et al.* (1999) and Adrian (2007). Their auto-generation mechanism postulates that a parent hairpin can produce a downstream hairpin vortex and a secondary hairpin vortex through induction and vortex roll-up. The present upstream transitional hairpin forest can certainly provide a sufficient number of parent hairpin vortices to start off the auto-generation process in the downstream turbulent region. Perry & Marusic

https://doi.org/10.1017/S0022112010004027 Published online by Cambridge University Press

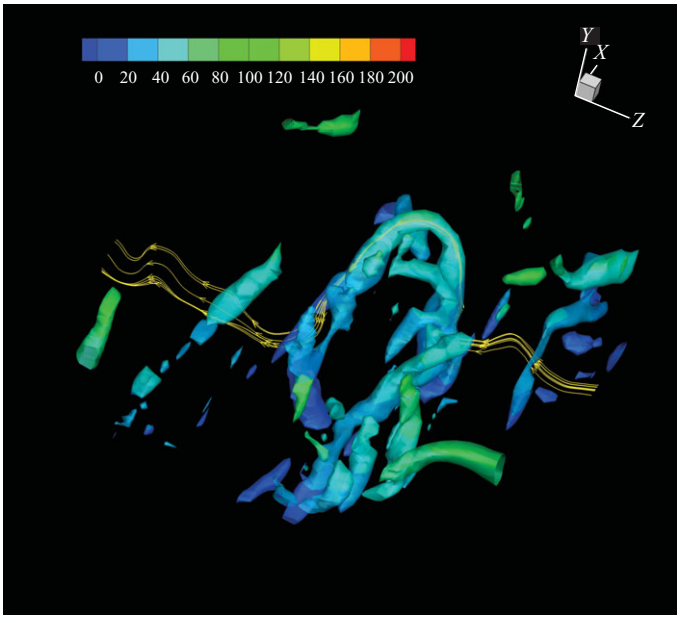


FIGURE 17. Zoomed view of the highlighted near-wall small structure in figure 16 overlaid with local instantaneous vortex lines. Iso-surfaces are coloured using y^+.

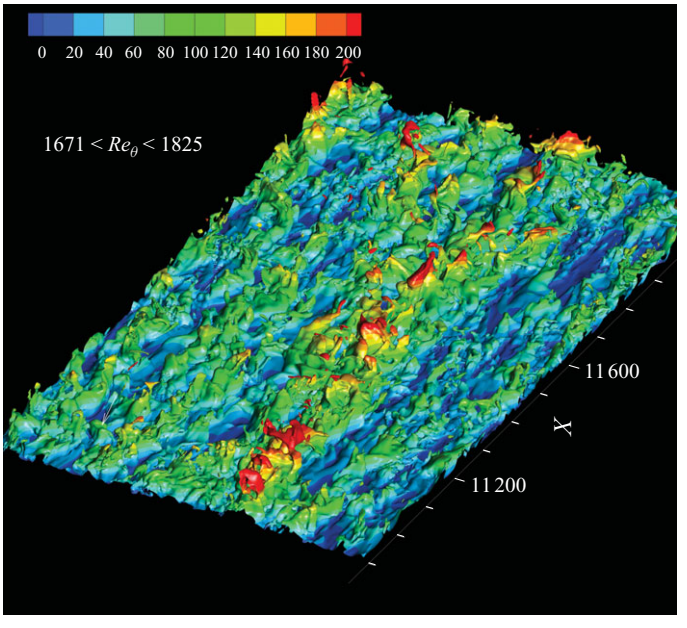


FIGURE 18. Near-wall small structures resolved by $\phi = 0.28$ in the boundary layer with passing wakes at $t = 46\mathscr{T}$. Iso-surfaces are coloured using y^+.

(1995), Marusic & Perry (1995) and Marusic (2001) investigated the scenario of hairpin packets as a boundary-layer-dominant structure by calculating Reynolds stresses and two-point correlations using an attached eddy model based on a superposition of these hairpin structures. Calculated results were evaluated against experimental

https://doi.org/10.1017/S0022112010004027 Published online by Cambridge University Press

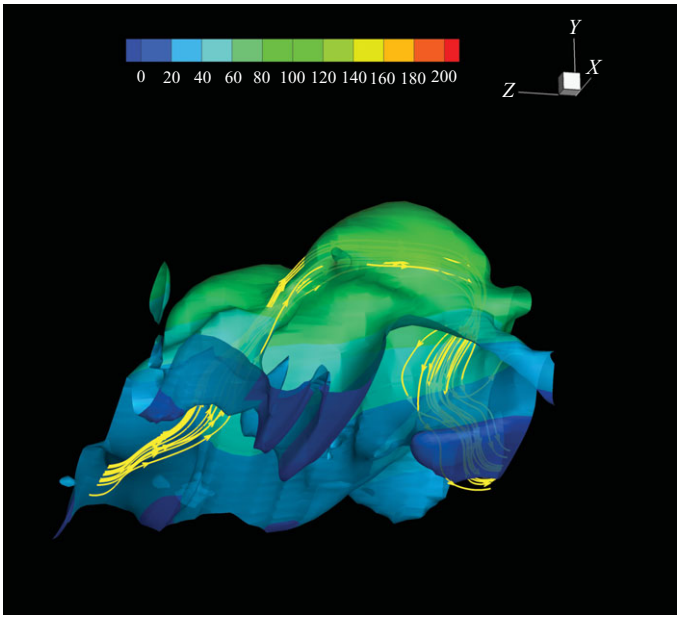


FIGURE 19. Zoomed view of the highlighted near-wall small structure in figure 18 overlaid with instantaneous local vortex lines. Iso-surfaces are coloured using y^+.

measurements. Their results are consistent with the notion that spatially coherent packets are statistically significant structures in the logarithmic region. The present DNS evidence for the initiation, growth and preponderance of small-scale hairpin vortices in the near-wall region lends support to their model.

7. Internal structures of infant turbulent spots

Early experimental studies on the growth of turbulent spots in the standard boundary layer can be found in, for example, Gad-el-Hak *et al.* (1981). Their spots were initiated by ejecting a small amount of fluid through a minute hole on the flat plate. They attributed the lateral growth of the spots to the combined effects from entrainment and destabilization. The growth by destabilization mechanism is related to the spot turbulence destabilizing the laminar boundary layer in its vicinity. Henningson, Spalart & Kim (1987) reported DNS studies on the growth of manufactured turbulent spots in a plane channel flow and flat-plate boundary layer. They found that the spreading angle and propagation velocities were similar in the two cases, but the turbulent arrowhead regions pointed in opposite directions. An additional difference is that the boundary-layer spot has an overhang at its leading edge, but the channel spot has only a slightly disturbed laminar region. Since their spots were generated artificially, there was neither merging between the spots nor catching up of the spots with the retreating continuous turbulent region, as in the present realistic transitional boundary layer. More recent DNS studies started to address the question of internal structures of artificially generated turbulent spots. Through blowing in flat-plate boundary layers, Krishnan & Sandham (2006) observed the presence of a large number of hairpin vortices inside the turbulent spots. They also found that the merging of laterally displaced spots created an inflectional velocity profile in the interaction zone which triggered new large-scale coherent structures.

https://doi.org/10.1017/S0022112010004027 Published online by Cambridge University Press

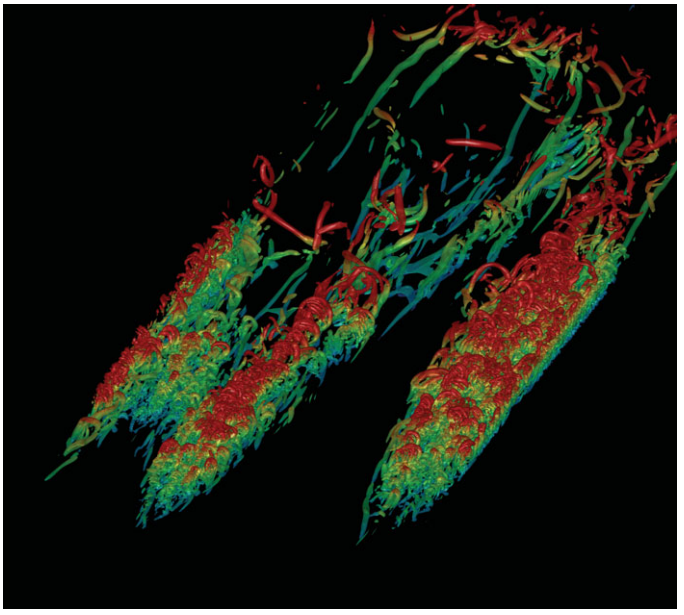


FIGURE 20. Iso-surfaces of the second invariant of the velocity gradient tensor $Q \approx 0$ in the boundary layer with passing wakes at $t = 38\mathscr{T}$ in the range of $1600 < x/\theta_0 < 3600$. The iso-surfaces are coloured based on local values of y/δ. Scales of y/δ are the same as in figure 13(c).

Our interest here regarding turbulent spots is their internal vortical structure rather than growth rate or geometrical characteristics. Figure 20 shows a few turbulent spots in the present passing-wake perturbed boundary layer at the instant of $t = 38\mathscr{T}$ in the region of $1600 < x/\theta_0 < 3600$. The turbulent spots shown here are qualitatively similar to those shown in figure 12 at $t = 46\mathscr{T}$. At the station of $x = 2000\theta_0$, $Re_\theta = 282$ and $\delta = 70\theta_0$. The streamwise extent of the turbulent spots shown in the figure is between 10 and 20 local boundary-layer thicknesses. In comparison, figure 3 of Gad-El-Hak *et al.* (1981) showed that at the end of their recording cycle the streamwise extent of their turbulent spot was approximately 15δ. The $Q \approx 0$ iso-surfaces of figure 20 demonstrate that hairpin vortices with a range of scales co-exist inside the spots, forming a hairpin forest. The heads of the larger hairpins protrude through the boundary-layer edge as suggested by the red colour of the structures. The present turbulent spots are also similar to those observed by Wu & Moin (2009, 2010), in which the free stream has isotropic turbulent patches. In figure 20, the structures shown in the upper right corner are those of the free-stream passing wakes. Now we turn our attention to infant turbulent spots and their generation.

The Blasius boundary layer in the work of Wu & Moin (2009) breaks down through a sequence of events. Disturbances from the free-stream isotropic turbulent patches induce quasi-spanwise structures; these spanwise structures develop into lambda-shaped structures inside the boundary layer; the joint portion of the lambda-shaped structures detaches resulting in a pair of obliquely oriented quasi-streamwise vortices; hairpin packets develop from the pair of quasi-streamwise vortices; the heads of the hairpins at the boundary-layer edge form aligned bulges in the streamwise direction, corresponding to a local pattern of alternating negative and positive fluctuating streamwise velocity; breakdown follows immediately.

https://doi.org/10.1017/S0022112010004027 Published online by Cambridge University Press

The events leading to the formation of the turbulent spots at $t = 38\mathscr{T}$ shown in figure 20 were recorded at eight consecutive instants in figure 21 starting from $t = 37.5\mathscr{T}$. Vortex structures are revealed using iso-surfaces of the second invariant of the velocity gradient tensor coloured by the local values of u/U_f. The red-coloured ($u/U_f \geqslant 1$) chaotic structures in the downstream portion of each subfigure are the fluctuations from the free-stream passing wakes. The iso-surface of $u/U_f = 0.4$ is also overlaid with the vortex structures to demonstrate the laminar non-chaotic nature of the local boundary layer prior to the onset of turbulent spots.

A few words regarding receptivity are in order. Hunt & Durbin (1999) advanced the traditional notion of shear sheltering, which essentially asserts that vortical disturbances in the free stream cannot easily penetrate the boundary layer for shear amplification. Jacobs & Durbin (1998) found that low-frequency modes can still penetrate the boundary layer. Thus, shear sheltering becomes shear filtering. These concepts are probably more relevant to the flow of Wu & Moin (2009, 2010) with free-stream blocks of isotropic turbulence than to the present boundary layer with passing wakes. Because the passing wakes contain mean flow directed towards the boundary layer (Durbin & Wu 2007), fluctuating structures are transported by the mean wake flow into the laminar boundary layer, and subsequently subjected to shearing action. Figure 21(*a–d*) shows the presence of quasi-streamwise vortices inside the boundary layer behind the free-stream passing wakes due to stretching of the transported fluctuating structures inside the layer. The importance of such quasi-streamwise vortices in bypass transition was emphasized in previous papers (e.g. see Henningson, Lundbladh & Johansson 1993). Adrian (2007) pointed out that these quasi-streamwise vortices are capable of acting like the wall-attached legs to induce an upward flow that rolls up into the arch of a hairpin vortex (see also Krishnan & Sandham 2006; Jocksch & Kleiser 2008). Figure 21(*e–h*) shows that hairpin packets do indeed emerge over the streamwise vortices. The head elements of the hairpin vortices in the packets protrude outside the boundary-layer edge as indicated by the red colour of the heads. The aligned hairpin vortices contained in a packet thus produce a local pattern of alternating negative and positive fluctuating streamwise velocity, as described by Wu & Moin (2009). The results shown in the figure demonstrate a close connection between the onset of infant turbulent spots and the formation of hairpin packets. As a matter of fact, the internal structure of an infant turbulent spot can be considered as a hairpin packet. The sequence of events leading to the onset of infant turbulent spots understood from this work is consistent with, but much more detailed and interesting than, that described 10 years ago in Wu *et al.* (1999).

8. Summary

Despite the fact that the present quasi-standard boundary layer is perturbed by migrating wakes with finite mean velocity directing obliquely towards the plate, and despite the fact that the wake turbulence is highly anisotropic and inhomogeneous, the three flow phenomena reported by Wu & Moin (2009, 2010) from a quasi-standard boundary layer with free-stream isotropic turbulent patches are demonstrated to be valid, and presumably general to a class of similar types of boundary layers. These flow physics features are a preponderance of hairpin vortices in the turbulent boundary-layer region up to $Re_\theta = 1850$, an overshoot of total shear stress in the transitional region, and a laminar breakdown process closely tied to the formation of hairpin packets. Furthermore, all the following observations are also equally applicable to both flows. The r.m.s. wall-shear stress fluctuation, $\tau'^{+}_{w,rms}$, is nearly constant in the

https://doi.org/10.1017/S0022112010004027 Published online by Cambridge University Press

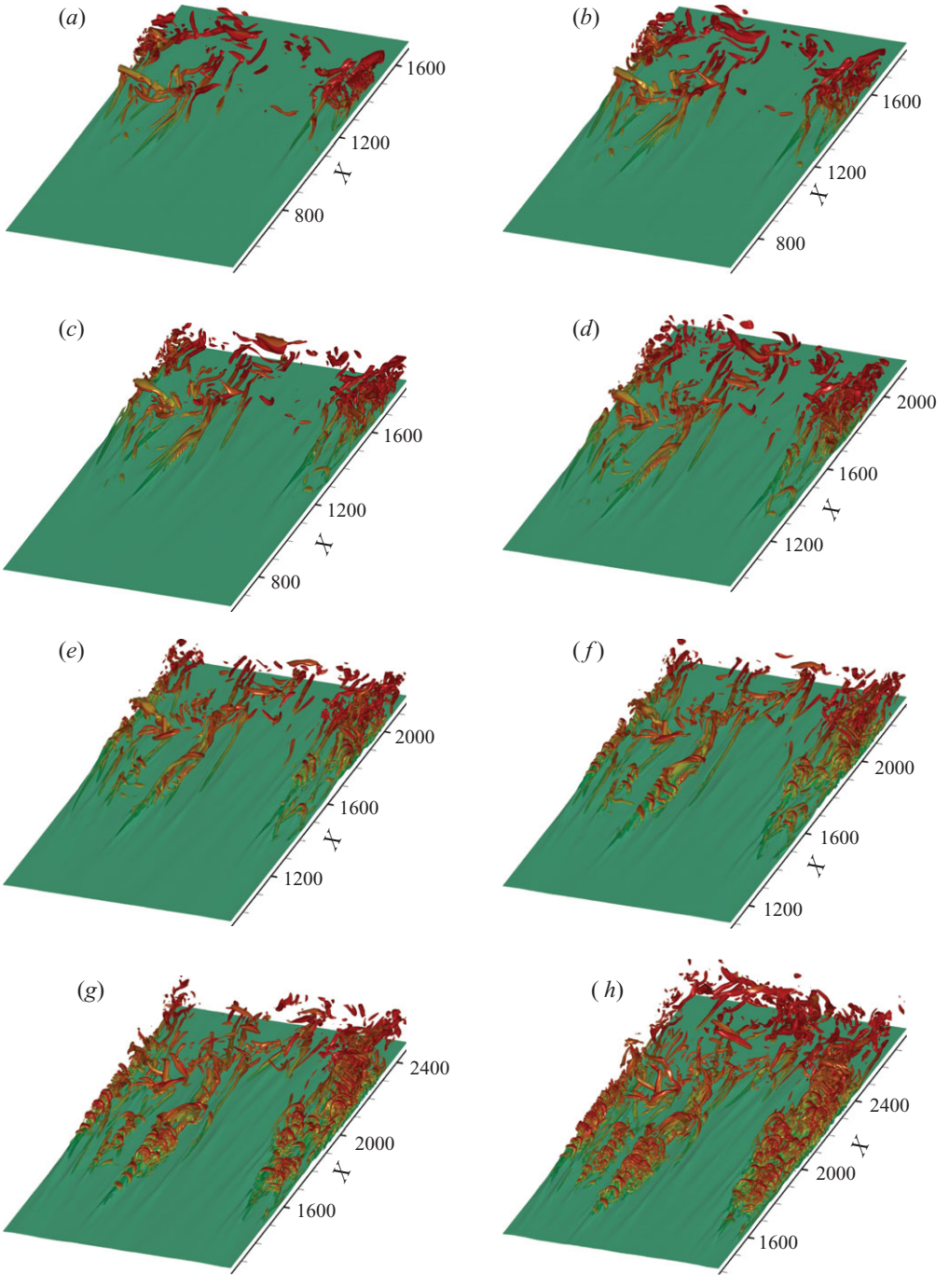


FIGURE 21. Iso-surfaces of the second invariant of the velocity gradient tensor $Q \approx 0$ overlaid with the iso-surfaces of $u/U_f = 0.4$. The iso-surfaces of Q are coloured based on local values of u/U_f with higher values represented by red, $0 < u/U_f < 1$. (*a*) $t = 37.5\mathscr{T}$, (*b*) $37.55\mathscr{T}$, (*c*) $37.6\mathscr{T}$, (*d*) $37.65\mathscr{T}$, (*e*) $t = 37.7\mathscr{T}$, (*f*) $37.75\mathscr{T}$, (*g*) $37.8\mathscr{T}$ and (*h*) $37.85\mathscr{T}$.

https://doi.org/10.1017/S0022112010004027 Published online by Cambridge University Press

turbulent boundary layer from $900 < Re_\theta < 1850$. The internal structure of merged turbulent spots is a hairpin forest, and the internal structure of infant turbulent spots is a hairpin packet. The total stress overshoot is associated with a localized streamwise acceleration of the streamwise velocity component in the transitional region. Aside from the hairpin forest in the outer and intermediate regions, in the near-wall region of the turbulent boundary layer, there also exist many small-scale hairpin vortices. This suggests that the preponderance of hairpin vortices in the turbulent boundary layer is not simply a result of the decayed remnants of the upstream transitional hairpin forest. Rather, young hairpin vortices are still being initiated from the very near-wall region up to $Re_\theta = 1850$, possibly under the auto-generation mechanism of Adrian (2007). Temperature iso-surfaces of the companion thermal boundary layer are found to be a useful tracer in visualizing boundary-layer hairpin vortex structures. By systematically adjusting the chosen temperature iso-surface value, hairpin vortices located at different wall-normal zones are readily revealed.

The passing period used in the present work is the same as that in Wu & Moin (2009, 2010). The chosen value is moderate in the sense that turbulent spots generated from one cycle catch up with, and merge into, the retreating continuous turbulent region within a short distance, thereby completing the bypass transition process. In the limiting case that the passing period is very large, bypass transition may not be completed within a reasonable distance, if at all, depending upon the Reynolds number. The other limiting case of very small passing period asymptotes the flow of boundary-layer transition under continuous free-stream isotropic turbulence, which was studied using DNS by Jacobs & Durbin (2001), Brandt, Schlatter & Henningson (2004), Ovchinnikov, Choudhari & Piomelli (2008). However, since those studies did not address the three main issues raised in this work, whether or not the generality of the associated phenomena can be extended to boundary layers subjected to continuous free-stream isotropic turbulence remains to be clarified. Overall, the results presented here have clarified, to a reasonable degree, one of the major issues raised in the article of Marusic (2009).

The computer program used in this study was developed by the late Dr C. D. Pierce of the Center for Turbulence Research at Stanford. This work was supported by an NSERC Discovery Grant, the Department of Defense Academic Research Program (ARP), and the Canada Research Chair Program (CRC). The simulations were performed at the High Performance Computing Virtual Laboratory (HPCVL). The kind assistance of the HPCVL staff is gratefully acknowledged.

REFERENCES

Adrian, R. J. 2007 Hairpin vortex organization in wall turbulence. *Phys. Fluids* **19**, 041301.

Adrian, R. J., Meinhart, C. D. & Tomkins, C. D. 2000 Vortex organization in the outer region of the turbulent boundary layer. *J. Fluid Mech.* **422**, 1–54.

Brandt, L., Schlatter, P. & Henningson, D. S. 2004 Transition in boundary layers subject to free-stream turbulence. *J. Fluid Mech.* **517**, 167–198.

Castillo, L., Araya, J. G., Meneveau, C. & Jansen, K. 2009 DNS of turbulent boundary layers with/without external pressure gradient based on a multi-scale, dynamic recycle inflow condition approach. *Bull. Am. Phys. Soc.* **54** (19), 60.

Chen, C. P. & Blackwelder, R. F. 1978 Large-scale motion in a turbulent boundary layer: a study using temperature contamination. *J. Fluid Mech.* **89**, 1–31.

Chow, Y. C., Uzol, O. & Katz J. 2002 Flow non-uniformities and turbulent 'hot spots' due to wake–blade and wake–wake interactions in a multistage turbomachine. *Trans. ASME: J. Turbomach.* **124**, 553–563.

https://doi.org/10.1017/S0022112010004027 Published online by Cambridge University Press

DeGraaff, D. B. & Eaton, J. K. 2000 Reynolds-number scaling of the flat-plate turbulent boundary layer. *J. Fluid Mech.* **422**, 319–346.

Durbin, P. A. & Wu, X. 2007 Transition beneath vortical disturbances. *Annu. Rev. Fluid Mech.* **39**, 107–128.

Gad-el-Hak M., Blackwelder, R. F. & Riley, J. J. 1981 On the growth of turbulent regions in laminar boundary layers. *J. Fluid Mech.* **110**, 73–95.

Gravante, S. P., Naguib, A. M., Wark, C. E. & Nagib, H. M. 1998 Characterization of the pressure fluctuations under a fully developed turbulent boundary layer. *AIAA J.* **36**, 1808–1816.

Henningson, D., Lundbladh, A. & Johansson, A. 1993 A mechanism for bypass transition from localized disturbances in wall-bounded shear flows. *J. Fluid Mech.* **250**, 169–207.

Henningson, D., Spalart, P. & Kim, J. 1987 Numerical simulations of turbulent spots in plane Poiseuille and boundary layer flow. *Phys. Fluids* **30**, 2914–2917.

Hunt, J. C. R. & Durbin, P. A. 1999 Perturbed shear layers and shear sheltering. *Fluid Dyn. Res.* **24**, 375–404.

Jacobs, R. G. & Durbin, P. A. 1998 Shear sheltering and the continuous spectrum of the Orr–Sommerfeld equation. *Phys. Fluids* **10**, 2006–2011.

Jacobs, R. G. & Durbin, P. A. 2001 Simulation of bypass transition. *J. Fluid Mech.* **428**, 185–212.

Jocksch, A. & Kleiser, L. 2008 Growth of turbulent spots in high-speed boundary layers on a flat plate. *Intl J. Heat Fluid Flow* **29**, 1543–1557.

Khujadze, G. & Oberlack, M. 2004 DNS and scaling laws from new symmetry groups of ZPG turbulent boundary layer flow. *Theor. Comput. Fluid Dyn.* **18**, 391441.

Kim, J. & Moin, P. 1986 The structure of the vorticity field in turbulent channel flow. Part 2. Study of ensemble-averaged fields. *J. Fluid Mech.* **162**, 339.

Krishnan, L. & Sandham, N. D. 2006 On the merging of turbulent spots in a supersonic boundary layer flow. *Intl J. Heat Fluid Flow* **27**, 542–550.

Lee, J. H. & Sung, H. J. 2009 Hairpin packet structure of a turbulent boundary layer in inclined wall-normal/spanwise planes. *Bull. Am. Phys. Soc.* **54** (19), 100.

Li, Q., Schlatter, P., Brandt, L. & Henningson, D. S. 2009 Direct numerical simulation of a spatially developing turbulent boundary layer with passive scalar transport. *Intl J. Heat Fluid Flow* **30**, 916–929.

Lund, T. S., Wu, X. & Squires, K. D. 1998 Generation of turbulent inflow data for spatially-developing boundary layer simulation *J. Comp. Phys.* **140**, 233–258.

Marusic, I. 2001 On the role of large-scale structures in wall turbulence. *Phys. Fluids.* **13**, 735–743.

Marusic, I. 2009 Unravelling the mechanisms of wall turbulence. *J. Fluid Mech.* **629**, 1–4.

Marusic, I. & Perry, A. E. 1995 A wall-wake model for the turbulence structure of boundary layers. Part 2. Further experimental support. *J. Fluid Mech.* **298**, 389–407.

Moin, P. & Kim, J. 1985 The structure of the vorticity field in turbulent channel flow. Part 1. Analysis of instantaneous fields and statistical correlations. *J. Fluid Mech.* **155**, 441–464.

Murlis, J., Tsai, H. M. & Bradshaw, P. 1982 The structure of turbulent boundary layers at low Reynolds numbers. *J. Fluid Mech.* **122**, 13–56.

Osterlund, J. M. 1999 Experimental studies of zero-pressure-gradient turbulent boundary layer flow. PhD thesis, Royal Institute of Technology, Stockholm, Sweden.

Ovchinnikov, V., Choudhari, M. M. & Piomelli, U. 2008 Numerical simulations of boundary-layer bypass transition due to high-amplitude free-stream turbulence. *J. Fluid Mech.* **613**, 135–169.

Perry, A. E. & Marusic, I. 1995 A wall-wake model for the turbulence structure of boundary layers. Part 1. Extension of the attached eddy hypothesis. *J. Fluid Mech.* **298**, 361–388.

Purtell, L. P., Klebanoff, P. S. & Buckley, F. T. 1981 Turbulent boundary layer at low Reynolds number. *Phys. Fluids* **24**, 802–811.

Schewe, G. 1983 On the structure and resolution of wall-pressure fluctuations associated with turbulent boundary layer flow. *J. Fluid Mech.* **134**, 311–328.

Schlatter, P., Orlu, R., Li, Q., Brethouwer, G., Fransson, J. H. M., Johansson, A. V., Alfredsson, P. H. & Henningson, D. S. 2009 Turbulent boundary layers up to $Re_\theta = 2500$ studied through simulation and experiment. *Phys. Fluids*, **21**, 051702.

Schubauer, G. B. & Skramstad, H. K. 1947 Laminar boundary layer oscillations and stability of laminar flow. *J. Aeronaut. Sci.* **14**, 69–78.

https://doi.org/10.1017/S0022112010004027 Published online by Cambridge University Press

Simens, M. P., Jimenez, J., Hoyas, S. & Mizuno, Y. 2009 A high-resolution code for turbulent boundary layers. *J. Comp. Phys.* **228**, 4218–4231.

Soranna, F., Chow, Y. C., Uzol, O. & Katz, J. 2006 The effect of Inlet Guide Vanes on the flow structure and turbulence around a rotor blade. *Trans. ASME: J. Turbomach.* **128**, 82–95.

Spalart, P. R. 1988 Direct simulation of a turbulent boundary layer up to $R_\theta = 1410$. *J. Fluid Mech.* **187**, 61–98.

Spalart, P. R. & Watmuff, J. H. 1993 Experimental and numerical study of a turbulent boundary layer with pressure gradients. *J. Fluid Mech.* **249**, 337–371.

Uzol, O., Chow, Y. C., Katz, J. & Meneveau, C. 2003 Average passage flow field and deterministic stresses in the tip and hub regions of a multi-stage turbomachine. *Trans. ASME: J. Turbomach.* **125**, 714–725.

Van Atta, C. W. & Helland, K. N. 1980 Exploratory temperature-tagging measurements of turbulent spots in a heated laminar boundary layer. *J. Fluid Mech.* **100**, 243–255.

Wallace, J. M. 2009 Twenty years of experimental and direct numerical simulation access to the velocity gradient tensor: what have we learned about turbulence? *Phys. Fluids* **21**, 021301.

Wu, X. & Durbin, P. A. 2000 Numerical simulation of heat transfer in a transitional boundary layer with passing wakes. *Trans. ASME J. Heat Transfer* **122**, 248–257.

Wu, X., Jacobs, R., Hunt, J. C. R. & Durbin, P. A. 1999 Simulation of boundary layer transition induced by periodically passing wakes. *J. Fluid Mech.* **398**, 109–153.

Wu, X. & Moin, P. 2008 A direct numerical simulation study on the mean velocity characteristics in turbulent pipe flow. *J. Fluid Mech.* **608**, 81–112.

Wu, X. & Moin, P. 2009 Direct numerical simulation of turbulence in a nominally zero-pressure-gradient flat-plate boundary layer. *J. Fluid Mech.* **630**, 5–41.

Wu, X. & Moin, P. 2010 Transitional and turbulent boundary layer with heat transfer. *Phys. Fluids* **22** (8), 085105.

Zhou, J., Adrian, R. J., Balachandar, S. & Kendall, T. M. 1999 Mechanisms for generating coherent packets of hairpin vortices in channel flow. *J. Fluid Mech.* **387**, 353–396.

https://doi.org/10.1017/S0022112010004027 Published online by Cambridge University Press